



Exploring the Lower Mass Gap and Unequal Mass Regime in Compact Binary Evolution

Michael Zevin¹ , Mario Spera^{1,2,3} , Christopher P L Berry^{1,4} , and Vicky Kalogera¹

¹ Center for Interdisciplinary Exploration and Research in Astrophysics (CIERA) and Department of Physics and Astronomy, Northwestern University, 1800 Sherman Ave., Evanston, IL 60201, USA; zevin@u.northwestern.edu

² Physics and Astronomy Department Galileo Galilei, University of Padova, Vicolo dell'Osservatorio 3, I-35122 Padova, Italy

³ INFN—Padova, Via Marzolo 8, I-35131 Padova, Italy

⁴ SUPA, School of Physics and Astronomy, University of Glasgow, Glasgow G12 8QQ, UK

Received 2020 July 2; revised 2020 July 15; accepted 2020 July 19; published 2020 August 5

Abstract

On 2019 August 14, the LIGO and Virgo detectors observed GW190814, a gravitational-wave signal originating from the merger of a $\simeq 23 M_{\odot}$ black hole (BH) with a $\simeq 2.6 M_{\odot}$ compact object. GW190814's compact-binary source is atypical both in its highly asymmetric masses and in its lower-mass component lying between the heaviest known neutron star (NS) and lightest known BH in a compact-object binary. If formed through isolated binary evolution, the mass of the secondary is indicative of its mass at birth. We examine the formation of such systems through isolated binary evolution across a suite of assumptions encapsulating many physical uncertainties in massive-star binary evolution. We update how mass loss is implemented for the neutronization process during the collapse of the proto-compact object to eliminate artificial gaps in the mass spectrum at the transition between NSs and BHs. We find it challenging for population modeling to match the empirical rate of GW190814-like systems while simultaneously being consistent with the rates of other compact binary populations inferred from gravitational-wave observations. Nonetheless, the formation of GW190814-like systems at any measurable rate requires a supernova engine model that acts on longer timescales such that the proto-compact object can undergo substantial accretion immediately prior to explosion, hinting that if GW190814 is the result of massive-star binary evolution, the mass gap between NSs and BHs may be narrower or nonexistent.

Unified Astronomy Thesaurus concepts: Gravitational waves (678); Gravitational wave sources (677); Neutron stars (1108); Stellar mass black holes (1611); Astrophysical black holes (98); Supernovae (1668); Core-collapse supernovae (304); Stellar evolutionary models (2046)

1. Introduction

The third observing run of the Advanced LIGO–Virgo network (Aasi et al. 2015; Acernese et al. 2015) has already yielded unprecedented discoveries: the most massive binary neutron star (BNS) system (Abbott et al. 2020a), and compact binaries with significantly asymmetric masses (Abbott et al. 2020b, 2020c). The most recently announced event, GW190814 (Abbott et al. 2020c), also had a compact-object component that lies within the observed gap in masses between neutron stars (NSs) and black holes (BHs), known as the lower mass gap (LMG; Bailyn et al. 1998; Özel et al. 2010, 2012; Farr et al. 2011). Since no tidal signatures are measurable in the gravitational-wave (GW) data and no electromagnetic or neutrino counterpart has been reported (Abbott et al. 2020c, and references therein), the nature of the lighter object in the binary is uncertain. Nonetheless, this event establishes that $\simeq 2.6 M_{\odot}$ compact objects do exist in binaries.

The majority of non-recycled NSs in the Galaxy have masses of $\sim 1.3 M_{\odot}$ (Özel et al. 2012; Kiziltan et al. 2013). However, the maximum mass that an NS can achieve, $m_{\text{NS}}^{\text{max}}$, is currently uncertain. The Galactic millisecond pulsar J0740+6620 has a Shapiro-delay mass measurement of $2.05\text{--}2.24 M_{\odot}$ (68% credibility; Cromartie et al. 2020); this has been updated to $1.95\text{--}2.13 M_{\odot}$ when analyzed using a population-informed prior (Farr & Chatziioannou 2020). The pulsar J1748–2021B has been estimated to have a mass of $2.52\text{--}2.95 M_{\odot}$ (68% confidence) assuming that the periastron precession is purely relativistic, but if there are contributions from the tidal or rotational distortion of the companion, this estimate would not be valid (Freire et al. 2008). GW190425's primary component had a mass greater than most Galactic NSs, $1.61\text{--}2.52 M_{\odot}$ (90%

credibility; Abbott et al. 2020a); while high NS masses of $\lesssim 2.5 M_{\odot}$ can be explained theoretically via stable accretion in low- and intermediate-mass X-ray binary (XRB) systems (e.g., Pfahl et al. 2003; Lin et al. 2011; Tauris et al. 2011), the explanation for a high-mass component in a BNS system is open to debate (e.g., Kruckow 2020; Romero-Shaw et al. 2020; Safarzadeh et al. 2020). These observational constraints provide key insights about the NS equation of state (EOS); although candidate EOSs for non-rotating NSs can have maximum masses that extend as high as $\sim 3 M_{\odot}$ (Rhoades & Ruffini 1974; Kalogera & Baym 1996; Müller & Serot 1996), population studies of known NSs (Alsing et al. 2018; Farr & Chatziioannou 2020), analysis of the tidal deformability of GW170817 (Abbott et al. 2018; Essick et al. 2020), modeling of the electromagnetic counterparts associated with GW170817 (Abbott et al. 2017a, 2017b; Cowperthwaite et al. 2017; Kasen et al. 2017; Margalit & Metzger 2017; Villar et al. 2017), and constraints from late-time observations of short gamma-ray bursts (Schroeder et al. 2020) suggest a maximum NS mass of $\lesssim 2.1\text{--}2.7 M_{\odot}$.

The upper end of the LMG is motivated by mass determinations in XRB systems. Though the lowest-mass BH candidate to date is between 2.6 and $6.1 M_{\odot}$ (95% confidence; Thompson et al. 2019, see also van den Heuvel & Tauris 2020), most BHs observed in the Galaxy have masses $\gtrsim 5 M_{\odot}$ (see, e.g., Miller & Miller 2015). Selection effects may be affecting the observational sample (Kreidberg et al. 2012), but it has been argued that such biases do not affect this broad picture (e.g., Özel et al. 2010).

A gap (or lack thereof) in the mass spectrum of compact objects offers insights into the underlying supernova (SN) mechanism responsible for their formation. In particular, if instability growth and launch of the SN proceed on rapid

timescales (~ 10 ms and ~ 100 ms, respectively), stellar modeling and hydrodynamic simulations predict a dearth in remnant masses between ~ 2 and $5 M_{\odot}$ (see Belczynski et al. 2012; Fryer et al. 2012; Müller et al. 2016). Alternatively, if instabilities are delayed and develop over longer timescales ($\gtrsim 200$ ms), accretion can occur on the proto-NS before the neutrino-driven explosion, and this gap would be filled (Fryer et al. 2012). The mass distributions of NSs and BHs observed in our Galaxy provided initial evidence that this phenomenon proceeds on rapid timescales, and such prescriptions were therefore inherited by many rapid population studies for NS and BH systems (e.g., Dominik et al. 2012; Belczynski et al. 2014, 2016; Breivik et al. 2016; Rodriguez et al. 2016; Giacobbo & Mapelli 2018; Mapelli & Giacobbo 2018; Kremer et al. 2019; Neijssel et al. 2019; Spera et al. 2019; Zevin et al. 2019; Banerjee et al. 2020; di Carlo et al. 2020; Rastello et al. 2020). However, recently discovered Galactic compact objects with mass estimates that extend inside the LMG (e.g., Thompson et al. 2019; Wyrzykowski & Mandel 2020) and population fits to known Galactic BNSs (Vigna-Gómez et al. 2018) raise tension with this interpretation; additional observations could further constrain SN physics (e.g., Breivik et al. 2019a).

GW190814 offers an unprecedented probe into the gap of compact object masses between BHs and NSs. The mass of the binary’s secondary component is $m_2 = 2.50\text{--}2.67 M_{\odot}$ (90% credibility), making it the heaviest NS or lightest BH ever identified in a compact-object binary. The secondary of GW190814 has the potential to provide insights into the SN explosion mechanism, because it is a relatively clean probe of the compact object’s mass at birth; even if the lighter component of GW190814 was the first-born compact object, only small amounts of accretion are possible over the evolutionary timescale of its more massive companion. Additionally, the more massive primary component is $m_1 \simeq 23 M_{\odot}$, making this the most asymmetric compact binary discovered, with a mass ratio of $q = m_2/m_1 \simeq 0.11$ (see Abbott et al. 2020b). Such low mass ratios are predicted to be rare in both the canonical isolated binary evolution (e.g., Dominik et al. 2012; Giacobbo & Mapelli 2018; Kruckow et al. 2018; Spera et al. 2019) and dynamical formation (e.g., Clausen et al. 2013; Rodriguez et al. 2019; Arca Sedda et al. 2020) scenarios for compact-binary formation.

We investigate compact-object formation in the LMG and the formation of highly asymmetric compact binaries. We focus on the formation of GW190814-like systems using various standard assumptions for binary evolution, and whether population models can produce such systems while being consistent with the empirical merger rates of different compact-binary populations. We do not make specific alterations to our population models to preferentially form GW190814-like systems, but instead explore how uncertain model parameters affect the formation rate and properties of such systems. In Section 2, we give an overview of our population models and present an updated prescription for determining remnant masses. We then discuss our model results in Section 3, including the merger rates and formation pathways of GW190814-like systems. We explain implications for binary evolution physics in Section 4. Throughout we assume solar metallicity of $Z_{\odot} = 0.017$ (Grevesse & Sauval 1998) and Planck 2015 cosmological parameters of $H_0 = 68 \text{ km s}^{-1} \text{ Mpc}^{-1}$, $\Omega_m = 0.31$, and $\Omega_{\Lambda} = 0.69$ (Ade et al. 2016).

2. Population Models

We use the rapid binary population synthesis code COSMIC (Breivik et al. 2019b) to examine the properties and rates of compact binaries.⁵ We investigate the impact of initial binary properties, efficiency of common envelope (CE) evolution, survival in the CE phase, the determination of remnant masses, and SN natal kick prescriptions. We describe COSMIC and our model assumptions in Appendix A, and our model variations are summarized in Table B1. Below we highlight updates to COSMIC that are pertinent to this work.

2.1. Remnant Mass Prescription

We follow the remnant mass prescriptions from Fryer et al. (2012) for determining the baryonic mass of the proto-compact object. The two prescriptions from Fryer et al. (2012), *Rapid* and *Delayed*, are used to map the results of hydrodynamical simulations to rapid population synthesis. The two models differ in their assumed instability growth timescale (~ 10 ms and ~ 200 ms for Rapid and Delayed, respectively), with the Rapid model naturally leading to a low-mass gap.

We make a small, but important, change when determining the final gravitational mass from the baryonic mass of the proto-compact object; further motivation and details are in Appendix A.2. Rather than assuming a fixed fractional mass loss of the total pre-SN mass for BHs as in Fryer et al. (2012), we cap the mass loss due to neutronization to 10% of the maximum mass assumed for the iron core, because hydrodynamical simulations show that the mass loss from neutrino emission is $\sim 10\%$ of the iron-core mass rather than the total baryonic mass of the compact-object progenitor (C. Fryer 2020, private communication). Combining this criterion with the baryonic-to-gravitational mass prescription from Lattimer & Yahil (1989) gives

$$M_{\text{grav}} = \begin{cases} \frac{20}{3} [(1 + 0.3M_{\text{bar}})^{1/2} - 1] \Delta M \leq 0.1 m_{\text{Fe}}^{\text{max}} \\ M_{\text{bar}} - 0.1 m_{\text{Fe}}^{\text{max}} & \text{otherwise} \end{cases}, \quad (1)$$

where $\Delta M = M_{\text{bar}} - M_{\text{grav}}$ and $m_{\text{Fe}}^{\text{max}}$ is the maximum possible mass assumed for the iron core, which we set to $5 M_{\odot}$. This upper limit on the BH mass loss when converting from baryonic to gravitational mass is slightly larger than, though qualitatively similar to, that in the procedure in Mandel & Müller (2020). Whether the compact remnant is an NS or a BH can then be determined by comparing M_{grav} to $m_{\text{NS}}^{\text{max}}$. We show the relation between zero-age main sequence (ZAMS) mass and remnant mass for both our SN prescriptions in Figure 1.

2.2. Merger Rates and Astrophysical Populations

Local merger rate densities can be determined from population synthesis to directly compare population predictions with the empirical rates measured by LIGO–Virgo. We calculate local merger rates of different compact binary populations in a similar manner to Giacobbo & Mapelli (2018) and Spera et al. (2019), as described in detail in Appendix B. For compact binary coalescence class i , the local merger rate (the merger rate at

⁵ cosmic-popsynth.github.io (Version 3.3).

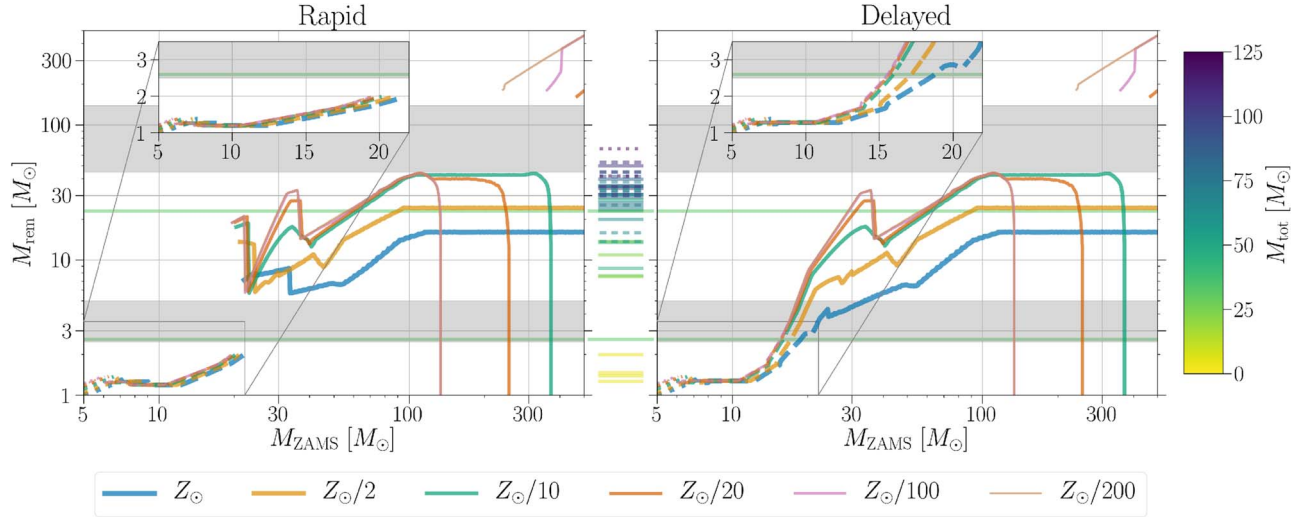


Figure 1. Relation between ZAMS mass and remnant mass for single stars in our models across a range of metallicities, using the Rapid (left) and Delayed (right) SN mechanisms for determining compact-object masses. White dwarfs, NSs, and BHs are distinguished by dotted, dashed, and solid lines, respectively; at low metallicities, the mass spectrum continues above the upper mass gap for high ZAMS masses. The approximate lower and upper mass gaps are highlighted with gray bands. Horizontal lines between the panels show the median component masses of compact binaries identified via GWs in the first catalog where they were reported with an astrophysical probability of $p_{\text{astro}} > 0.5$: the LIGO Scientific Collaboration and Virgo Collaboration catalog (solid lines; Abbott et al. 2019a, 2020a, 2020b, 2020c), the Institute for Advanced Studies catalog (dashed lines; Venumadhav et al. 2019, 2020), and the Open Gravitational-wave Catalog (dotted lines; Nitz et al. 2019, 2020); the components of GW190814 are also shown in the left and right panels and inset panels as a light green horizontal line. Both components in an individual system are colored by their total mass.

redshifts $z \leq z_{\text{loc}} = 0.01$) across all metallicity models j is

$$\mathcal{R}_{\text{loc},i} = \frac{1}{t_1(z_{\text{loc}})} \int_0^{z_{\text{max}}} \psi(z) \sum_j p(Z_j|z) f_{\text{loc},i}(z, Z_j) \frac{dt_1}{dz} dz, \quad (2)$$

where t_1 is the lookback time, $\psi(z)$ is the star formation rate density, $p(Z_j|z)$ is the likelihood of metallicity Z_j at redshift z , $f_{\text{loc},i}(z, Z_j)$ is the mass fraction of systems born at redshift z with metallicity Z_j that merge in the local universe, and $z_{\text{max}} = 15$ is the maximum redshift we consider for binary formation.

To get a representative astrophysical population of compact binary mergers, we combine the information from across metallicities for each population model. We assume that all systems merge at the median measured redshift of GW190814 ($z \simeq 0.053$).⁶ The delay time of each system thus provides its formation time and formation redshift. We then give a weight to each system based on the mass-weighted star formation weight (Equation (B3)) at the formation redshift, the metallicity distribution (Equation (B5)) at the formation redshift, the relative formation efficiency for the double compact object population in question in the particular metallicity model, and the relative number of systems formed in a particular metallicity model. Drawing a subset of systems based on these weights gives a representative sample at the merger redshift of GW190814.

3. Results

We explore the properties and rates of compact binaries in our population models, focusing on how standard population modeling and variations of physical assumptions inherent to binary stellar evolution impact the formation rate of asymmetric-mass binaries and mergers with components residing in

the LMG, especially GW190814-like systems. Given the uncertainty in $m_{\text{NS}}^{\text{max}}$, we show combined distributions for all systems with at least one component having a mass $> 3 M_{\odot}$ unless otherwise specified.

3.1. Probing the Regime of Low Mass Ratio

We find that merger rates drop precipitously as component masses become more asymmetric, in agreement with many other population synthesis studies (e.g., Dominik et al. 2012; Kruckow et al. 2018; Mapelli & Giacobbo 2018; Neijssel et al. 2019, though see also Eldridge & Stanway 2016; Eldridge et al. 2017). Figure 2 shows the distribution of mass ratio and total mass in a subset of our populations, with contour lines marking 90%, 99%, and 99.9% of the population. Mass ratios are concentrated near unity for large total masses; since the pair instability process limits the maximum mass of BHs (e.g., Woosley 2017; Farmer et al. 2019; Marchant et al. 2019), the degree of possible asymmetry decreases as a function of total mass. For systems with lower total mass, the mass ratio distribution extends to more asymmetric configurations, reaching down to $q \lesssim 0.1$.

We do not see a strong difference in the distributions of total mass and mass ratio when varying the efficiency of CE ejection. However, for the Rapid SN mechanism we find fewer mass ratios near $q \sim 0.4$, and an island at lower mass ratios, whereas there is a continuum for the Delayed SN mechanism. This is a byproduct of the LMG that is inherent to the Rapid prescription; because this gap extends from ~ 3 to $6 M_{\odot}$, a system with $M_{\text{tot}} = 18 M_{\odot}$ cannot have a mass ratio between ~ 0.2 and 0.5 . However, even with the Delayed SN mechanism we find $\sim 90\%$ of systems to have mass ratios of $q \gtrsim 0.4$. Regardless of our model assumptions, we find GW190814's mass ratio and total mass to be an outlier, lying close to the 99.9% contour for our populations.

⁶ The low merger redshift of GW190814 makes these results a good proxy for local mergers in general.

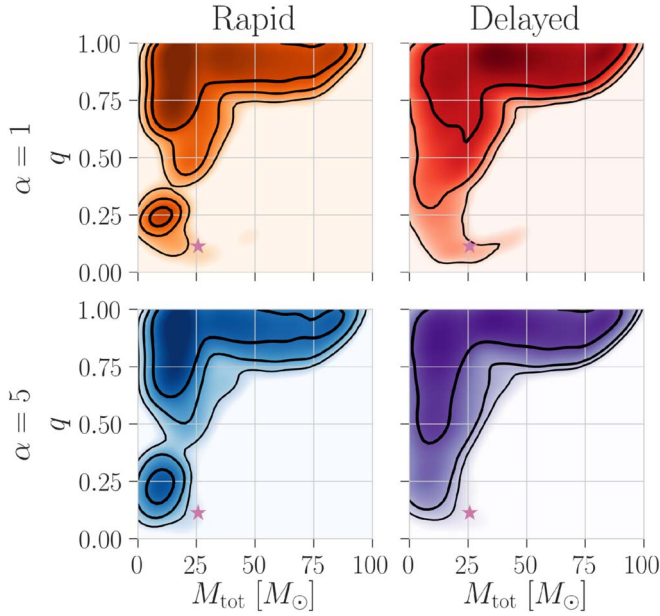


Figure 2. Distributions of total mass $M_{\text{tot}} = m_1 + m_2$ and mass ratio $q = m_2/m_1$ ($m_2 \leq m_1$) of astrophysical populations for models varying the CE efficiency α and remnant-mass prescription. For the other model variations, we use initial conditions from Sana et al. (2012), the bimodal natal-kick model, and the Pessimistic assumption for CE survival (see Appendix A.1). We include all systems with at least one component having $m > 3 M_\odot$. Systems are drawn from metallicity models based on the star formation history and metallicity evolution outlined in Section 2.2, assuming they merge at the redshift of GW190814. Densities are log-scaled, with contours containing 90%, 99%, and 99.9% of systems. GW190814’s M_{tot} and q are shown with a pink star; error bars are present, but are smaller than the marker.

3.2. Populating the LMG

The impact of the LMG is more apparent when examining systems’ component masses. Figure 3 shows the primary and secondary masses of systems merging at the redshift of GW190814 for a subset of our populations. Systems are more sparse when moving away from equal mass. Although rare, we do find systems matching GW190814’s component masses when using the Delayed prescription, which naturally populates the LMG. However, it is *impossible* to form GW190814-like systems in our models using the Rapid SN prescription.

In Figure 4, we show cumulative distributions for the mass ratio and secondary mass in our populations. In the full population, we find that one in $\sim 10^3$ systems have a mass ratio similar to GW190814 or lower ($q \leq 0.12$). For systems with a secondary mass $\leq 3 M_\odot$, $\approx 8\%$ of systems have a mass ratio of $q \leq 0.12$, though this drops to $\approx 0.7\%$ when a more efficient CE is assumed, which is qualitatively similar to findings from other population synthesis work (e.g., Giacobbo & Mapelli 2018). For systems with a secondary mass $> 3 M_\odot$, the mass ratio distribution deviates significantly when assuming the Rapid SN mechanism compared to the Delayed mechanism. We find $\lesssim 0.03\%$ of these systems have mass ratios of $q \leq 0.12$ with a Delayed SN mechanism, whereas these systems are nonexistent when assuming a Rapid SN mechanism. The LMG can be seen in the bottom panel of Figure 4 as a plateau in the Rapid models as a function of m_2 ; the Delayed models, which populate the gap, have a more gradual buildup. For Delayed models, GW190814’s secondary mass lies at about the ninth percentile of the full population for $\alpha = 5$, and drops to about the first percentile for $\alpha = 1$.

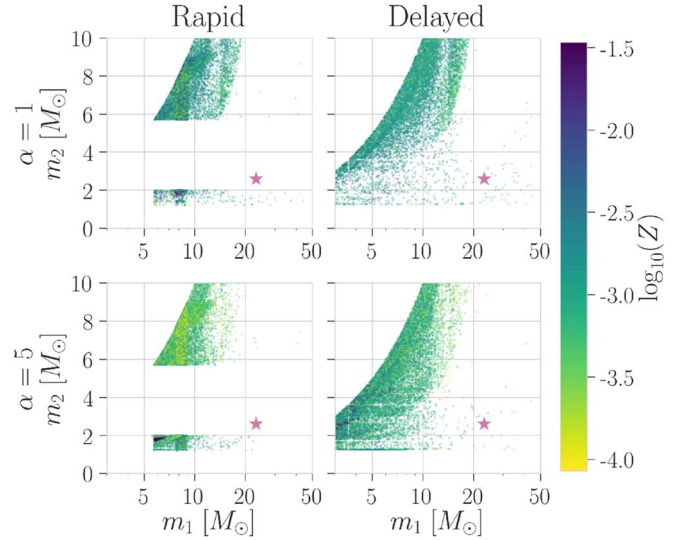


Figure 3. Primary mass m_1 and secondary mass m_2 for the same models as in Figure 2. Systems are colored by their metallicity. GW190814’s component masses are shown with a pink star; error bars are again smaller than the marker.

3.3. Compact Binary Merger Rates

Merger rates are a useful diagnostic for comparing predictions of population synthesis modeling to the empirical merger rate estimated by the LIGO Scientific & Virgo Collaboration (LVC). Figure 5 shows local merger rates of different compact binary populations for four variations of model assumptions. To compare with LVC rates, we assume that compact objects with masses $\leq 3 M_\odot$ are NSs, and those with masses $> 3 M_\odot$ are BHs. For the four models examined, we find binary black hole (BBH), neutron star–black hole (NSBH), and BNS merger rates to be consistent with the measured LVC rate (bands for BBHs and BNSs, upper limit for NSBHs). We do not expect exact agreement in rates, since the LVC results were calculated using mass distributions that are different from our populations.

The single-event rate for GW190814-like systems is $1\text{--}23 \text{ Gpc}^{-3} \text{ yr}^{-1}$ (90% credible level; Abbott et al. 2020c), and is shown with a pink band in Figure 5. To compare our model predictions with the empirical rate, we choose two approximations for identifying GW190814-like systems in our models: a *Narrow* GW190814-like rate where we choose systems with $0.06 \leq q \leq 0.16$ and $20 \leq M_{\text{tot}}/M_\odot \leq 30$ (pink stars) and a *Broad* GW190814-like rate where we choose systems with $q \leq 0.2$ and $M_{\text{tot}}/M_\odot \geq 20$. In both cases, we find the local merger rate of GW190814-like systems to be over an order of magnitude lower than the empirical GW190814 rate. For example, in our model with a Delayed SN mechanism and $\alpha = 1$, we find a local merger rate of $0.08 \text{ Gpc}^{-3} \text{ yr}^{-1}$ for our Broad GW190814-like assumption and $0.04 \text{ Gpc}^{-3} \text{ yr}^{-1}$ for our Narrow GW190814-like assumption; for a more efficient CE, the Broad and Narrow rates drop by factors of 1.8 and 2.4, respectively. Merger rates for our other model variations are presented in Table B1.

3.4. Formation of GW190814-like Systems

We identify two main channels for forming GW190814-like systems through isolated binary evolution in our population models. These can be broadly categorized as Channel A, where the primary (more massive) star at ZAMS becomes the more

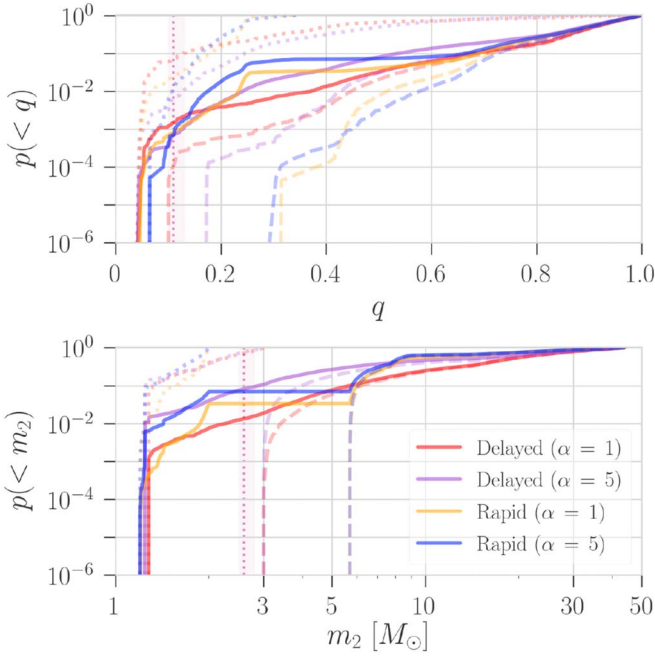


Figure 4. Cumulative distribution function for the mass ratio q and secondary mass m_2 for the same models presented in Figure 2. Solid lines show the combined population for all systems containing at least one component with $m > 3 M_\odot$, whereas dashed and dotted lines show the corresponding cumulative distribution functions for the BBH ($m_1 > 3 M_\odot$, $m_2 > 3 M_\odot$) and NSBH ($m_1 > 3 M_\odot$, $m_2 \leq 3 M_\odot$) populations, respectively. The dotted pink line and shaded region show the median and 90% credible interval for GW190814.

massive BH component in the compact binary, and Channel B, where the primary star at ZAMS becomes the less massive object in the compact binary (either an NS or a BH). Figure 6 shows evolutionary diagrams for examples from these general channels.

In Channel A, the binary typically starts as a $>30 M_\odot$ primary and $>12 M_\odot$ secondary at ZAMS. The binary evolves without interaction during the main sequence of the primary. At core helium burning, the primary overflows its Roche lobe. Depending on the mass ratio at the time, the mass transfer will proceed either stably or unstably, in the latter case triggering a CE phase (Taam & Sandquist 2000). The primary then directly collapses into a $\sim 20 M_\odot$ BH. As the secondary crosses the Hertzsprung gap, it overflows its Roche lobe and proceeds through highly non-conservative mass transfer. Since the mass ratio between the donor star and the already-formed BH is close to unity, this phase of mass transfer typically proceeds stably. The naked helium-star does not proceed through another phase of mass transfer and becomes an NS following its SN. These systems generally have large orbital separations at double compact-object formation, and thus to merge within a Hubble time the newly formed NS needs to be kicked into a highly eccentric orbit, typically with a post-SN eccentricity of $\gtrsim 0.9$.

In Channel B, the binary starts with a ZAMS mass ratio of $0.45 \lesssim q \lesssim 0.7$. The primary fills its Roche lobe while on the main sequence. This phase of stable mass transfer donates a significant amount of material to the secondary, leading to a mass inversion where the lighter star at ZAMS becomes the more massive star. The initially more massive star forms the lighter compact object before the secondary leaves the main sequence. Due to the large mass asymmetry between the

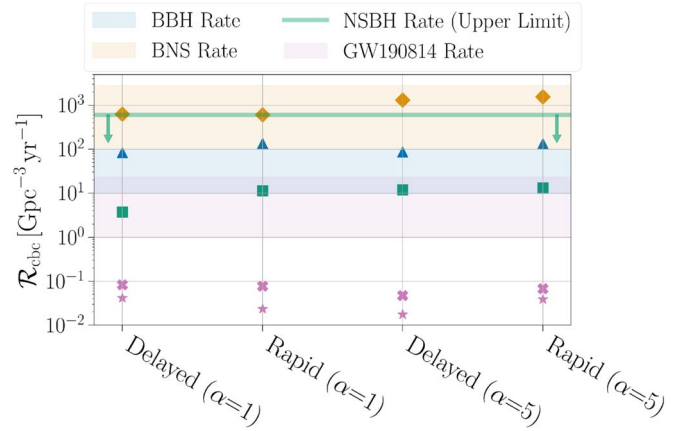


Figure 5. Local merger rates for models where we vary the CE efficiency and remnant mass prescription. The blue and orange shaded regions mark the 90% credible level for the current empirical BBH (Abbott et al. 2019a) and BNS (Abbott et al. 2020a) merger rates from the LVC, respectively, the green line marks the 90% credible upper limit for the LVC NSBH rate (Abbott et al. 2019a), and the pink shaded region marks the 90% credible single-event rate for GW190814-like systems (Abbott et al. 2020c). Matching colored symbols mark the BBH (blue triangles), BNS (orange diamonds), and NSBH (green squares) merger rates from our models, assuming $m_{\text{NS}}^{\text{max}} = 3 M_\odot$. Pink symbols mark the merger rates from our models for systems with $q \leq 0.2$ and $M_{\text{tot}}/M_\odot \geq 20$ (crosses), and $0.06 \leq q \leq 0.16$ and $20 \leq M_{\text{tot}}/M_\odot \leq 30$ (stars).

already-formed NS and the now more massive secondary, when the secondary evolves into a giant and overflows its Roche lobe, mass transfer proceeds unstably and initiates a CE. The binary significantly hardens during the CE phase, and the second star directly collapses into a BH. This channel for forming GW190814-like systems was also identified in Mandel et al. (2020), though in our case it does not necessitate an Optimistic CE scenario, and we still find systems from this channel when binaries with unstable mass transfer from Hertzsprung gap donors are assumed to merge.

At low metallicities, these channels operate with similar probability. For metallicities of $Z \leq Z_\odot/30$, we find that 57% of systems in our simulated population with $0.06 \leq q \leq 0.16$ and $20 \leq M_{\text{tot}}/M_\odot \leq 30$ lead to the primary ZAMS star becoming the heavier compact object, whereas 43% lead to the secondary ZAMS star becoming the heavier compact object. At higher metallicities ($Z > Z_\odot/30$) Channel A becomes dominant, with 73% of systems proceeding through Channel A and 27% through Channel B. As the metallicity increases to $\gtrsim Z_\odot/8$, GW190814-like systems no longer form since BH masses are suppressed due to line-driven winds. Since there are only a small number of GW190814-like systems in our models, the channels presented here and their relative likelihood only offer a broad picture of how systems with properties similar to GW190814 form.

4. Discussion and Conclusions

GW190814 is a GW event that challenges compact binary population modeling and places new constraints on the physics of massive-star evolution. We explore the formation of compact binary mergers with highly asymmetric masses and components residing in the LMG. We find that systems with properties similar to GW190814 *can* form through isolated binary evolution; however, the predicted formation rates of such systems are *an order of magnitude lower* than the empirical single-event rate when considering models that match

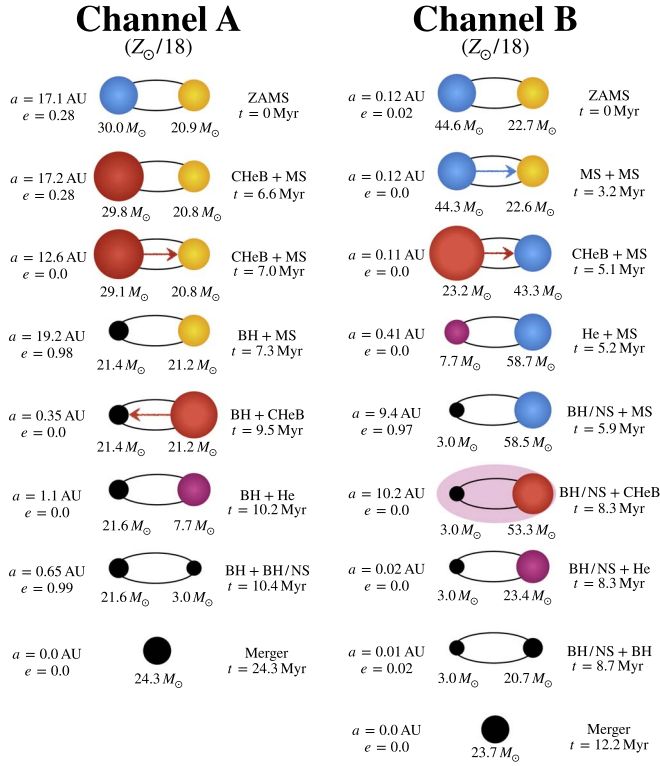


Figure 6. Evolutionary diagrams of two systems following the dominant pathways for forming GW190814-like systems in our models, as described in Section 3.4. In Channel A, the more massive star at ZAMS becomes the larger compact object, whereas in Channel B the system undergoes a mass inversion and the more massive star at ZAMS evolves into the lighter compact object. Stable mass transfer is denoted by an arrow from the donor to the accretor, and a CE phase in Channel B by the pink oval surrounding the two stars.

the observed rates for other compact binary populations. The mass of GW190814’s secondary lies in the dearth of compact objects between the heaviest NSs and lightest BHs, and *if* it is the result of isolated binary evolution, requires that instability growth and SN launch proceed on longer timescales than typically assumed.

The most massive Galactic NSs have low-mass stellar companions, allowing for stable mass accretion on significant timescales. Thus, the masses of these NSs are not a direct probe of their masses at formation. GW190814’s lower-mass component likely had minimal accretion after formation: its mass at merger is indicative of its birth mass. Even if there was a mass inversion in the system and the secondary component of GW190814 was the first-born compact object (Channel B in Section 3.4), the amount of material it could feasibly accrete is limited by the evolutionary timescale of its massive companion (which goes on to form a $\gtrsim 20 M_\odot$ BH). The amount accreted by an NS or BH at the Eddington limit is

$$\Delta M_{\text{Edd}} \approx 0.03 \left(\frac{R}{10 \text{ km}} \right) \left(\frac{t}{1 \text{ Myr}} \right) M_\odot, \quad (3)$$

where R is the radius of the compact object (e.g., Cameron & Mock 1967). Thus, even for accretion timescales of $\mathcal{O}(1 \text{ Myr})$ and reasonable NS radii (Abbott et al. 2018; Miller et al. 2019; Riley et al. 2019), the amount of mass that the lighter compact object could accrete is $\approx 0.03 M_\odot$, far too low to bridge the gap between the canonical $1.3 M_\odot$ NS mass and the $\approx 2.6 M_\odot$

secondary of GW190814. While there is evidence of super-Eddington accretion in ultraluminous X-ray sources (e.g., Bachetti et al. 2014), it is unlikely that this could increase the mass of GW190814’s lower-mass component significantly; the post-hydrogen exhaustion lifetime for the progenitor star of a $\approx 23 M_\odot$ BH is only $\sim 0.5 \text{ Myr}$, and mass transfer between the high-mass companion star and the already-formed compact object would almost assuredly be unstable due to the system’s large mass ratio. Thus, even at 10 times the Eddington rate, GW190814’s lower-mass component would not accrete more than $\mathcal{O}(0.1 M_\odot)$ during the remaining lifetime of its stellar companion.

As a clean probe of the natal mass of a compact object in the LMG, GW190814 is an exquisite system for constraining the SN mechanisms that impact remnant masses. The secondary’s mass is inconsistent with instability growth and SN launch on rapid timescales ($t \sim 10 \text{ ms}$; e.g., Fryer et al. 2012; Müller et al. 2016); if GW190814’s source formed from isolated binary evolution, it favors SN launch models where instabilities develop over a longer timescale ($t \sim 100 \text{ ms}$). As we only consider two SN models, we cannot place a lower limit on the instability growth timescale. More detailed hydrodynamical simulations investigating instability growth, SN launch, and how they connect to compact remnant masses (e.g., Ertl et al. 2020; Patton & Sukhbold 2020) will be needed to determine a lower limit on the timescales necessary to produce systems with component masses in the LMG, and whether there is a critical growth timescale that leads to a populated LMG. Semi-analytic prescriptions and fitting formulae based on these detailed models can then be adopted by rapid population synthesis, using either deterministic or probabilistic (e.g., Mandel & Müller 2020) approaches.

The combination of a highly asymmetric binary with a low-mass secondary is predicted to be rare in most rapid binary population studies (e.g., Dominik et al. 2012; Giacobbo & Mapelli 2018; Kruckow et al. 2018; Mapelli & Giacobbo 2018; Mapelli et al. 2019; Neijssel et al. 2019; Spera et al. 2019; Olejak et al. 2020), though population modeling that allows for unlimited super-Eddington accretion onto BHs finds that compact binaries with $q \sim 0.1$ have rates comparable to near-equal-mass mergers (Eldridge & Stanway 2016; Eldridge et al. 2017) and may be able to better match the mass asymmetry of GW190814. Even when we consider SN mechanisms that fill the LMG, our predicted rate for GW190814-like systems is in tension with the empirical LVC rate. There are many theoretical uncertainties in binary stellar evolution with complex correlations that strongly affect the rates and population properties of compact binary mergers (e.g., Barrett et al. 2018), and we only choose a few to investigate. It is possible that variations in other uncertain physical prescriptions, such as the mass-transfer accretion rates, mass-transfer efficiency, the criteria for the onset of unstable mass transfer, and how each of these depends on the evolutionary stages of the stars involved, may help to alleviate the discrepancy between the merger rates of GW190814-like systems and those of other compact binary populations. Observations of compact binaries with unusual properties (such as GW190814) will be paramount in constraining uncertainties in this high-dimensional parameter space.

This work focuses on the formation of systems with high mass ratios and component masses in the LMG through

canonical isolated binary evolution. Many other channels have been proposed for producing the compact binary mergers observed by LIGO–Virgo. Dynamical formation in dense stellar clusters such as globular clusters preferentially produces compact binaries with similar masses (e.g., Sigurdsson & Hernquist 1993), and thus the formation of NSBHs and other compact binaries with highly asymmetric masses is predicted to be rare (Clausen et al. 2013; Arca Sedda et al. 2020; Ye et al. 2020). While hierarchical mergers of NSs have been proposed as a means of populating the LMG (Gupta et al. 2020), this scenario is unlikely since heavier BHs dominate the dynamical interactions in clusters (e.g., Samsing & Hotokezaka 2020; Ye et al. 2020). The formation of compact binaries with highly asymmetric masses may be more prevalent in young star clusters (e.g., di Carlo et al. 2019; Rastello et al. 2020; Santoliquido et al. 2020), but Fragione & Banerjee (2020) finds the merger rate of NSBH systems in young massive and open clusters to be three orders of magnitude lower, similar to the predictions from old globular clusters. Other formation mechanisms have been explored for forming highly asymmetric compact binary mergers and mergers with components in the LMG, such as hierarchical systems in the galactic field (e.g., Antonini et al. 2017; Silsbee & Tremaine 2017; Fragione & Kocsis 2019; Safarzadeh et al. 2019; Fragione et al. 2020), hierarchical systems in galactic nuclei with a supermassive BH as the outer perturber (e.g., Antonini & Perets 2012; Petrovich & Antonini 2017; Hoang et al. 2018; Fragione et al. 2019; Stephan et al. 2019), and in disks around supermassive BHs in active galactic nuclei (e.g., McKernan et al. 2019; Yang et al. 2019). However, the rates and formation properties from these channels are uncertain. Nevertheless, a full picture of compact-binary mergers will require consideration of all these channels and investigation of how physical prescriptions (such as the connection between the underlying SN mechanism and remnant mass) jointly affect population properties, rates, and branching ratios across these channels (e.g., Stevenson et al. 2017; Talbot & Thrane 2017; Vitale et al. 2017; Zevin et al. 2017; Arca Sedda et al. 2020). The identification of bona fide NSBH systems and other compact-binary mergers with highly asymmetric masses will further constrain the relative contribution of various formation channels and the underlying physics of these formation pathways.

The authors thank Chris Fryer, Pablo Marchant, and Ilya Mandel for useful discussions, and we thank the anonymous referee for helpful suggestions that improved this paper. M.Z. acknowledges support from CIERA and Northwestern University. M.S. acknowledges funding from the European Union’s Horizon 2020 research and innovation program under the Marie-Sklodowska-Curie grant agreement No. 794393. C.P.L.B. is supported by the CIERA Board of Visitors Professorship. V.K. is supported by a CIFAR G+EU Fellowship and Northwestern University. This work used computing resources at CIERA funded by NSF grant No. PHY-1726951, and resources and staff provided for the Quest high performance computing facility at Northwestern University, which is jointly supported by the Office of the Provost, the Office for Research, and Northwestern University Information Technology.

*Software:*COSMIC (Breivik et al. 2019b), iPython (Pérez & Granger 2007), Matplotlib (Hunter 2007),

NumPy (Oliphant 2006; van der Walt et al. 2011), Pandas (McKinney 2010), SciPy (Virtanen et al. 2020).

Appendix A Population Models

COSMIC (Breivik et al. 2019b) is based on the single-star fitting formulae from Hurley et al. (2000) and binary evolution prescriptions from Hurley et al. (2002). Among many updates, COSMIC includes state-of-the-art physical prescriptions for stellar winds in massive stars (Vink et al. 2001) and stripped stars (Vink & de Koter 2005; Yoon & Langer 2005), multiple treatments for the onset (Belczynski et al. 2008; Claeys et al. 2014) and evolution (Claeys et al. 2014) of unstable mass transfer, multiple prescriptions for SN natal kicks (Hobbs et al. 2005; Bray & Eldridge 2016; Giacobbo & Mapelli 2020) with special treatment for electron-capture SNe (Podsiadlowski et al. 2004) and ultra-stripped SNe (Tauris et al. 2015), as well as mass loss and orbital evolution from pulsational pair instabilities and pair instability SNe (Woosley 2017, 2019; Marchant et al. 2019). Furthermore, COSMIC includes a number of variations for how initial conditions are sampled (Sana et al. 2012; Moe & di Stefano 2017), which can significantly affect the properties and rates of compact binary populations. Rather than simulating a predetermined number of systems, COSMIC runs populations specifically targeted at particular configurations of stellar types (such as BNSs or BBHs that merge within a Hubble time) until properties of the target population (such as their masses and orbital periods at formation) have converged (Breivik et al. 2019b), thereby adequately exploring the tails of population distributions.

A.1. Model Assumptions

We investigate five uncertain aspects of binary evolution physics.

1. Initial conditions (primary mass, mass ratio, orbital period, and eccentricity) are sampled either independently using the best-fit values from Sana et al. (2012) with a binary fraction of 0.7, or using the correlated multidimensional distributions from Moe & di Stefano (2017). In the multidimensional sampling, the binary fraction is determined based on the probability that a system with a given primary mass is in a binary.
2. CE efficiency, which determines how easily the envelope is unbound from the system during a CE phase, is parameterized as in Webbink (1984) and de Kool (1990). We vary the efficiency parameter α , using either $\alpha = 1$ or a higher value of $\alpha = 5$ (Fragos et al. 2019; Giacobbo & Mapelli 2019), and use a variable prescription for the envelope binding energy factor λ (Claeys et al. 2014). A higher CE efficiency will lead to wider post-CE binaries.
3. CE survival is chosen to be either an Optimistic or a Pessimistic scenario. In the Optimistic case, stars that overfill their Roche lobes on the Hertzsprung gap and proceed through unstable mass transfer are assumed to survive the CE phase, whereas in the Pessimistic case these systems are assumed to merge (see Belczynski et al. 2008). The Pessimistic scenario leads to significantly fewer compact binary mergers, particularly for BBHs.
4. Remnant masses are determined using the Rapid and Delayed prescriptions from Fryer et al. (2012). The Rapid prescription yields a mass gap between NSs and BHs,

whereas the Delayed prescription fills this gap (Figure 1). These prescriptions are updated as described in Section 2.1 and Appendix A.2.

5. SN natal kicks are determined in two ways. In the bimodal prescription, iron core-collapse SNe kicks are drawn from a Maxwellian distribution with a dispersion of $\sigma = 265 \text{ km s}^{-1}$ (Hobbs et al. 2005), whereas electron-capture SNe and ultra-stripped SNe are given weaker kicks drawn from a Maxwellian distribution with a dispersion of $\sigma = 20 \text{ km s}^{-1}$ (e.g., Podsiadlowski et al. 2004; van den Heuvel 2007; Tauris et al. 2015; Beniamini & Piran 2016, see Breivik et al. 2019b for more details). The second kick prescription uses the scaling based on compact-object mass and mass loss in Giacobbo & Mapelli (2020).

These represent only a few of the binary evolution parameters that can possibly affect the parameter distribution and merger rates of compact-binary populations. Besides the parameter variations described above, we anticipate that mass transfer conservation and the stellar-type specific criteria for the onset of unstable mass transfer will have the largest impact. In this study, we assume that mass transfer is limited to the thermal timescale of the accretor for stars and limited to the Eddington rate for compact objects, and that angular momentum is lost from the system as if the excess material is a wind from the accretor (Hurley et al. 2002). The onset of unstable mass transfer is determined as in Belczynski et al. (2008) using critical mass ratios for a given stellar type: $q_{\text{crit}} = 3.0$ for H-rich stars ($k_* = 1-6$), $q_{\text{crit}} = 1.7$ for helium main-sequence stars ($k_* = 7$), $q_{\text{crit}} = 3.5$ for evolved helium stars ($k_* = 8, 9$), and $q_{\text{crit}} = 0.628$ for compact objects ($k_* \geq 10$). A full exploration of parameter space is reserved for future work.

A.2. Remnant Mass Prescription

Here, we provide more details regarding the updated remnant mass prescription used in this study. To determine the mass of compact remnants, we follow the Rapid and Delayed prescriptions described in Fryer et al. (2012). These allow for the results of hydrodynamical simulations exploring the timescale of instability growth and launch of the SN to be used directly in rapid population synthesis. Mass fallback is also accounted for in the determination of the baryonic mass of the proto-compact object. As in Giacobbo & Mapelli (2020), we adjust the initial mass of the proto-compact object to be $1.1 M_\odot$ rather than $1.0 M_\odot$, as this better reproduces the typical masses of NSs in the Galaxy.

Following the determination of the baryonic mass of the remnant, the gravitational mass is calculated to account for neutronization in the collapsing core. In Fryer et al. (2012), the gravitational mass of the remnant is calculated differently for NSs and BHs. For NSs, the gravitational mass is calculated according to Lattimer & Yahil (1989) based on the neutrino observations of SN 1987A:

$$M_{\text{grav}} = \frac{20}{3} [(1 + 0.3M_{\text{bar}})^{1/2} - 1], \quad (\text{A1})$$

where M_{bar} is the pre-collapse baryonic mass calculated as in Fryer et al. (2012). For BHs the mass reduction is assumed to be a fixed percentage of the proto-compact object's baryonic

mass:

$$M_{\text{grav}} = 0.9M_{\text{bar}}. \quad (\text{A2})$$

This leads to an increasing amount of mass loss when converting from baryonic to gravitational mass as a function of increasing BH mass. Since the true maximum NS mass is unknown and likely sensitive to other aspects of the proto-compact object such as rotation, the delineation between these two prescriptions is typically determined by an adjustable parameter for the maximum NS mass: $m_{\text{NS}}^{\text{max}}$.

There are two issues with this simple prescription that affect the compact-object mass spectrum. First, the final mass of a BH remnant is a function of the *total* pre-collapse baryonic mass of the proto-compact object, though neutronization is instead occurring in the iron core of the proto-compact object. Even for massive BHs and hot radiation-supported cores, the iron core mass is $\lesssim 5 M_\odot$ (C. Fryer 2020, private communication). Hydrodynamical simulations show that the mass loss from neutrino emission is $\sim 10\%$ of this core mass rather than the total baryonic mass of the BH progenitor (C. Fryer 2020, private communication). Second, using separate prescriptions for determining NS and BH gravitational mass leads to an artificial gap in the mass spectrum; this artificial gap is different than the LMG and is apparent even when using the Delayed remnant mass prescription. For example, assuming $m_{\text{NS}}^{\text{max}} = 2.5 M_\odot$ and 10% mass loss when converting from baryonic to gravitational mass in BHs, the most massive NS that can be formed is $2.5 M_\odot$ whereas the least massive BH that can be formed is $2.7 M_\odot$.

With these in mind, we update how the final gravitational mass of a compact object is determined:

$$M_{\text{grav}} = \begin{cases} \frac{20}{3} [(1 + 0.3M_{\text{bar}})^{1/2} - 1] & \Delta M \leq 0.1 m_{\text{Fe}}^{\text{max}} \\ M_{\text{bar}} - 0.1 m_{\text{Fe}}^{\text{max}} & \text{otherwise} \end{cases}, \quad (\text{A3})$$

where $\Delta M = M_{\text{bar}} - M_{\text{grav}}$ and $m_{\text{Fe}}^{\text{max}}$ is the maximum possible mass of the iron core, which we set to $5 M_\odot$. For $m_{\text{Fe}}^{\text{max}} = 5 M_\odot$, the switchover in this conditional occurs at $\simeq 3.1 M_\odot$. As shown in Figure 1, this update eliminates any artificial gaps in the mass spectrum between NSs and BHs when using the Delayed SN mechanism.

Appendix B Local Merger Rates

The mass fraction of binaries that are born at redshift z and merge as compact binaries in the local universe is

$$f_{\text{loc},i}(z) = \frac{M_i(z; z_{\text{merge}} < z_{\text{loc}})}{M_{\text{samp}}}, \quad (\text{B1})$$

where M_{samp} is the total stellar mass sampled in the simulation, i represents the class of compact binary merger (BNS, NSBH, BBH, etc.), M_i is the stellar mass that leads to merger type i , and z_{loc} is the maximum redshift that we consider for local mergers, which we set to $z_{\text{loc}} = 0.01$. COSMIC accounts for the total mass sampled in M_{samp} , incorporating both the binary fraction and the mass contribution from lower-mass stars that do not lead to compact-binary formation. The number of mergers per unit volume that form in the redshift interval

Table B1
Population Model Assumptions and Local Merger Rates across All Simulated Models

Initial conditions	Model Assumptions			Natal kicks	Local Merger Rates ($\text{Gpc}^{-3} \text{yr}^{-1}$)					GW190814 Broad
	CE survival	CE efficiency (α)	Remnant mass		BBH $m_1 > 3 M_\odot$ $m_2 > 3 M_\odot$	NSBH $m_1 > 3 M_\odot$ $m_2 \leq 3 M_\odot$	BNS $m_1 \leq 3 M_\odot$ $m_2 \leq 3 M_\odot$	GW190814 Narrow		
MdS2017	Optimistic	1.0	Delayed	GM2020	2.0×10^3	2.3×10^2	1.4×10^3	2.4×10^{-1}	5.0×10^{-1}	
MdS2017	Optimistic	1.0	Delayed	Bimodal	1.2×10^3	2.1×10^1	1.0×10^3	2.8×10^{-1}	9.1×10^{-1}	
MdS2017	Optimistic	1.0	Rapid	GM2020	2.3×10^3	4.4×10^2	1.4×10^3	6.0×10^{-1}	1.3×10^0	
MdS2017	Optimistic	1.0	Rapid	Bimodal	1.6×10^3	2.3×10^2	1.0×10^3	3.1×10^{-1}	7.7×10^{-1}	
MdS2017	Optimistic	5.0	Delayed	GM2020	6.9×10^3	1.1×10^3	8.9×10^3	4.8×10^0	6.8×10^0	
MdS2017	Optimistic	5.0	Delayed	Bimodal	4.6×10^3	2.0×10^2	4.6×10^3	3.1×10^0	7.4×10^0	
MdS2017	Optimistic	5.0	Rapid	GM2020	6.7×10^3	4.2×10^2	8.4×10^3	7.1×10^0	1.2×10^1	
MdS2017	Optimistic	5.0	Rapid	Bimodal	5.7×10^3	2.7×10^2	5.0×10^3	3.0×10^0	5.6×10^0	
MdS2017	Pessimistic	1.0	Delayed	GM2020	3.6×10^2	4.4×10^1	1.0×10^3	3.7×10^{-2}	6.4×10^{-2}	
MdS2017	Pessimistic	1.0	Delayed	Bimodal	2.4×10^2	5.5×10^0	8.5×10^2	5.8×10^{-2}	1.2×10^{-1}	
MdS2017	Pessimistic	1.0	Rapid	GM2020	4.0×10^2	5.5×10^1	1.0×10^3	6.0×10^{-2}	1.5×10^{-1}	
MdS2017	Pessimistic	1.0	Rapid	Bimodal	3.1×10^2	2.6×10^1	7.7×10^2	5.0×10^{-2}	1.2×10^{-1}	
MdS2017	Pessimistic	5.0	Delayed	GM2020	4.8×10^2	1.4×10^2	2.8×10^3	9.1×10^{-2}	1.6×10^{-1}	
MdS2017	Pessimistic	5.0	Delayed	Bimodal	2.8×10^2	2.0×10^1	1.7×10^3	5.1×10^{-2}	9.4×10^{-2}	
MdS2017	Pessimistic	5.0	Rapid	GM2020	4.4×10^2	4.5×10^1	3.1×10^3	1.2×10^{-1}	2.0×10^{-1}	
MdS2017	Pessimistic	5.0	Rapid	Bimodal	3.7×10^2	2.5×10^1	2.1×10^3	7.7×10^{-2}	1.0×10^{-1}	
S+2012	Optimistic	1.0	Delayed	GM2020	1.2×10^3	1.3×10^2	1.0×10^3	1.5×10^{-1}	2.4×10^{-1}	
S+2012	Optimistic	1.0	Delayed	Bimodal	7.2×10^2	1.1×10^1	8.1×10^2	2.0×10^{-1}	6.2×10^{-1}	
S+2012	Optimistic	1.0	Rapid	GM2020	1.5×10^3	1.7×10^2	1.1×10^3	2.6×10^{-1}	5.5×10^{-1}	
S+2012	Optimistic	1.0	Rapid	Bimodal	1.0×10^3	7.0×10^1	7.9×10^2	1.0×10^{-1}	3.6×10^{-1}	
S+2012	Optimistic	5.0	Delayed	GM2020	2.4×10^3	5.1×10^2	5.0×10^3	9.8×10^{-1}	1.5×10^0	
S+2012	Optimistic	5.0	Delayed	Bimodal	1.6×10^3	7.2×10^1	3.1×10^3	5.8×10^{-1}	1.4×10^0	
S+2012	Optimistic	5.0	Rapid	GM2020	2.3×10^3	1.8×10^2	5.1×10^3	1.3×10^0	2.2×10^0	
S+2012	Optimistic	5.0	Rapid	Bimodal	2.0×10^3	7.7×10^1	3.4×10^3	4.7×10^{-1}	1.0×10^0	
S+2012	Pessimistic	1.0	Delayed	GM2020	1.7×10^2	3.3×10^1	7.9×10^2	4.9×10^{-2}	7.7×10^{-2}	
S+2012	Pessimistic	1.0	Delayed	Bimodal	8.4×10^1	3.7×10^0	6.3×10^2	4.1×10^{-2}	8.3×10^{-2}	
S+2012	Pessimistic	1.0	Rapid	GM2020	2.0×10^2	3.3×10^1	8.7×10^2	4.6×10^{-2}	9.7×10^{-2}	
S+2012	Pessimistic	1.0	Rapid	Bimodal	1.3×10^2	1.1×10^1	6.0×10^2	2.3×10^{-2}	7.7×10^{-2}	
S+2012	Pessimistic	5.0	Delayed	GM2020	1.7×10^2	9.4×10^1	1.7×10^3	3.8×10^{-2}	5.9×10^{-2}	
S+2012	Pessimistic	5.0	Delayed	Bimodal	8.6×10^1	1.1×10^1	1.3×10^3	1.7×10^{-2}	4.7×10^{-2}	
S+2012	Pessimistic	5.0	Rapid	GM2020	1.5×10^2	3.1×10^1	2.0×10^3	3.9×10^{-2}	6.3×10^{-2}	
S+2012	Pessimistic	5.0	Rapid	Bimodal	1.3×10^2	1.3×10^1	1.5×10^3	3.9×10^{-2}	6.7×10^{-2}	

Note. BBH, NSBH, and BNS rates are highlighted in green if they are within the empirical 90% credible bounds from LIGO–Virgo in Abbott et al. (2019b, 2019a, 2020a), respectively, are highlighted in orange if they are a factor of 2 above or below the 90% credible bounds, and are highlighted in red otherwise. The following abbreviations are used for sampling of initial conditions and natal kicks: MdS2017 for the multidimensional initial conditions from Moe & di Stefano (2017), S+2012 for the independent initial conditions from Sana et al. (2012), and GM2020 for the kick prescription from Giacobbo & Mapelli (2020). Narrow and Broad rates for GW190814-like systems are described in Section 3.3.

$[z, z + \Delta z]$ and merge in the local universe is thus

$$\Delta \mathcal{N}_{\text{loc},i}(z) = \psi(z) f_{\text{loc},i}(z) \frac{dt_1}{dz} \Delta z, \quad (\text{B2})$$

where $\psi(z)$ is the star formation rate density and $t_1(z)$ is the lookback time at redshift z . We use Madau & Fragos (2017) for the star formation rate density as a function of redshift,

$$\psi(z) = 10^{-2} \frac{(1+z)^{2.6}}{1 + [(1+z)/3.2]^{6.2}} M_{\odot} \text{ yr}^{-1} \text{ Mpc}^{-3}. \quad (\text{B3})$$

Integrating over all formation redshifts up to z_{max} , and converting to the number of mergers per unit time, gives us the local merger rate density

$$\begin{aligned} \mathcal{R}_{\text{loc},i} &= \frac{1}{t_1(z_{\text{loc}})} \int_0^{z_{\text{max}}} \psi(z) f_{\text{loc},i}(z) \frac{dt_1}{dz} dz \\ &= \frac{1}{H_0 t_1(z_{\text{loc}})} \int_0^{z_{\text{max}}} \frac{\psi(z) f_{\text{loc},i}(z)}{(1+z)E(z)} dz, \end{aligned} \quad (\text{B4})$$

with $E(z) = [\Omega_{\text{rad}}(1+z)^4 + \Omega_{\text{m}}(1+z)^3 + \Omega_{\text{k}}(1+z)^2 + \Omega_{\Lambda}]^{1/2}$. In practice, we discretize this integral with 1000 log-spaced redshift bins between z_{loc} and z_{max} . We consider systems out to $z_{\text{max}} = 15$ because systems born at earlier times make up only $\approx 1\%$ of the cumulative star formation and can thus be neglected.

Each population is run at a single metallicity and allows all binaries to evolve for the entire age of the universe, allowing for rate calculations to be performed in post-processing. We simulate 16 log-spaced metallicities between $Z_{\odot}/200$ and $2Z_{\odot}$ for each population model assumption. To account for metallicity evolution over cosmic time, we use the mean mass-weighted metallicity as a function of redshift in Madau & Fragos (2017),

$$\log_{10} \langle Z/Z_{\odot} \rangle = 0.153 - 0.074 z^{1.34}, \quad (\text{B5})$$

and assume a truncated log-normal distribution of metallicities at each redshift with a dispersion of 0.5 dex (Bavera et al. 2020) that reflects over boundaries at $Z_{\text{min}} = Z_{\odot}/200$ and $Z_{\text{max}} = 2Z_{\odot}$. The weights for each metallicity model j at a given redshift $p(Z_j|z)$ (which are normalized to unity to account for our discrete metallicity models, $\sum_j p(Z_j|z) = 1$) are then folded into the rate calculation to give a local volumetric merger rate across all metallicity models,

$$\mathcal{R}_{\text{loc},i} \simeq \frac{1}{H_0 t_1(z_{\text{loc}})} \sum_k \frac{\psi(\bar{z}_k) \sum_j p(Z_j|\bar{z}_k) f_{\text{loc},i}(\bar{z}_k, Z_j)}{(1 + \bar{z}_k) E(\bar{z}_k)} \Delta z_k, \quad (\text{B6})$$

where \bar{z}_k is the midpoint (in log space) of the k th redshift bin and Δz_k is the size of the k th redshift bin.

Local merger rates for each population model we simulate are shown in Table B1. In addition to BBH, NSBH, and BNS rates for each model, we also give a Narrow rate for GW190814-like systems (defined as $0.06 \leq q \leq 0.16$, $20 \leq M_{\text{tot}}/M_{\odot} \leq 30$) and a Broad rate for GW190814-like systems (defined as $q \leq 0.2$, $M_{\text{tot}}/M_{\odot} \geq 20$).

ORCID iDs

Michael Zevin  <https://orcid.org/0000-0002-0147-0835>
Mario Spera  <https://orcid.org/0000-0003-0930-6930>

Christopher P L Berry  <https://orcid.org/0000-0003-3870-7215>

Vicky Kalogera  <https://orcid.org/0000-0001-9236-5469>

References

- Aasi, J., Abbott, B. P., Abbott, R., et al. 2015, *CQGr*, **32**, 074001
 Abbott, B. P., Abbott, R., Abbott, T. D., et al. 2017a, *ApJL*, **848**, L12
 Abbott, B. P., Abbott, R., Abbott, T. D., et al. 2017b, *ApJL*, **850**, L39
 Abbott, B. P., Abbott, R., Abbott, T. D., et al. 2018, *PhRvL*, **121**, 161101
 Abbott, B. P., Abbott, R., Abbott, T. D., et al. 2019a, *PhRvX*, **9**, 31040
 Abbott, B. P., Abbott, R., Abbott, T. D., et al. 2019b, *ApJL*, **882**, L24
 Abbott, B. P., Abbott, R., Abbott, T. D., et al. 2020a, *ApJL*, **892**, L3
 Abbott, B. P., Abbott, R., Abbott, T. D., et al. 2020b, arXiv:2004.08342
 Abbott, R., Abbott, T. D., Abraham, S., et al. 2020c, *ApJL*, **896**, L44
 Acernese, F., Agathos, M., Agatsuma, K., et al. 2015, *CQGr*, **32**, 024001
 Ade, P., Aghanim, N., Arnaud, M., et al. 2016, *A&A*, **594**, A13
 Alsing, J., Silva, H. O., & Bert, E. 2018, *MNRAS*, **478**, 1377
 Antonini, F., & Perets, H. B. 2012, *ApJ*, **757**, 27
 Antonini, F., Toonen, S., & Hamers, A. S. 2017, *ApJ*, **841**, 77
 Arca Sedda, M., Mapelli, M., Spera, M., Benacquista, M., & Giacobbo, N. 2020, *ApJ*, **894**, 133
 Bachetti, M., Harrison, F. A., Walton, D. J., et al. 2014, *Natur*, **514**, 202
 Bailyn, C. D., Jain, R. K., Coppi, P., & Orosz, J. A. 1998, *ApJ*, **499**, 367
 Banerjee, S., Belczynski, K., Fryer, C. L., et al. 2020, *A&A*, **639**, A41
 Barrett, J. W., Gaebel, S. M., Neijssel, C. J., et al. 2018, *MNRAS*, **477**, 4685
 Bavera, S. S., Fragos, T., Qin, Y., et al. 2020, *A&A*, **635**, A97
 Belczynski, K., Buonanno, A., Cantiello, M., et al. 2014, *ApJ*, **789**, 120
 Belczynski, K., Kalogera, V., Rasio, F. A., et al. 2008, *ApJS*, **174**, 223
 Belczynski, K., Repetto, S., Holz, D. E., et al. 2016, *ApJ*, **819**, 108
 Belczynski, K., Wiktorowicz, G., Fryer, C. L., Holz, D. E., & Kalogera, V. 2012, *ApJ*, **757**, 91
 Beniamini, P., & Piran, T. 2016, *MNRAS*, **456**, 4089
 Bray, J. C., & Eldridge, J. J. 2016, *MNRAS*, **461**, 3747
 Breivik, K., Chatterjee, S., & Andrews, J. J. 2019a, *ApJL*, **878**, L4
 Breivik, K., Coughlin, S., Zevin, M., et al. 2019b, arXiv:1911.00903
 Breivik, K., Rodriguez, C. L., Larson, S. L., Kalogera, V., & Rasio, F. A. 2016, *ApJL*, **830**, 1
 Cameron, A. G., & Mock, M. 1967, *Natur*, **215**, 464
 Claeys, J. S. W., Pols, O. R., Izzard, R. G., Vink, J., & Verbunt, F. W. M. 2014, *A&A*, **563**, A83
 Clausen, D., Sigurdsson, S., & Chernoff, D. F. 2013, *MNRAS*, **428**, 3618
 Cowperthwaite, P. S., Berger, E., Villar, V. A., et al. 2017, *ApJL*, **848**, L17
 Cromartie, H. T., Fonseca, E., Ransom, S. M., et al. 2020, *NatAs*, **4**, 72
 de Kool, M. 1990, *ApJ*, **358**, 189
 di Carlo, U. N., Giacobbo, N., Mapelli, M., et al. 2019, *MNRAS*, **487**, 2947
 di Carlo, U. N., Mapelli, M., Giacobbo, N., et al. 2020, arXiv:2004.09525
 Dominik, M., Belczynski, K., Fryer, C., et al. 2012, *ApJ*, **759**, 52
 Eldridge, J. J., & Stanway, E. R. 2016, *MNRAS*, **462**, 3302
 Eldridge, J. J., Stanway, E. R., Xiao, L., et al. 2017, *PASA*, **34**, e058
 Ertl, T., Woosley, S. E., Sukhbold, T., & Janka, H.-T. 2020, *ApJ*, **890**, 51
 Essick, R., Landry, P., & Holz, D. E. 2020, *PhRvD*, **101**, 63007
 Farmer, R., Renzo, M., de Mink, S. E., Marchant, P., & Justham, S. 2019, *ApJ*, **887**, 53
 Farr, W. M., & Chatziioannou, K. 2020, *RNAAS*, **4**, 65
 Farr, W. M., Sravan, N., Cantrell, A., et al. 2011, *ApJ*, **741**, 103
 Fragione, G., & Banerjee, S. 2020, arXiv:2006.06702
 Fragione, G., Grishin, E., Leigh, N. W. C., Perets, H. B., & Perna, R. 2019, *MNRAS*, **488**, 2825
 Fragione, G., & Kocsis, B. 2019, *MNRAS*, **486**, 4781
 Fragione, G., Loeb, A., & Rasio, F. A. 2020, *ApJL*, **895**, L15
 Fragos, T., Andrews, J. J., Ramirez-Ruiz, E., et al. 2019, *ApJL*, **883**, L45
 Freire, P. C. C., Ransom, S. M., Bégin, S., et al. 2008, *ApJ*, **675**, 670
 Fryer, C. L., Belczynski, K., Wiktorowicz, G., et al. 2012, *ApJ*, **749**, 91
 Giacobbo, N., & Mapelli, M. 2018, *MNRAS*, **480**, 2011
 Giacobbo, N., & Mapelli, M. 2019, *MNRAS*, **482**, 2234
 Giacobbo, N., & Mapelli, M. 2020, *ApJ*, **891**, 141
 Grevesse, N., & Sauval, A. J. 1998, *SSRv*, **85**, 161
 Gupta, A., Gerosa, D., Arun, K. G., et al. 2020, *PhRvD*, **101**, 103036
 Hoang, B.-M., Naoz, S., Kocsis, B., Rasio, F. A., & Dosopoulou, F. 2018, *ApJ*, **856**, 140
 Hobbs, G., Lorimer, D. R., Lyne, A. G., & Kramer, M. 2005, *MNRAS*, **360**, 974
 Hunter, J. D. 2007, *CSE*, **9**, 99
 Hurley, J. R., Pols, O. R., & Tout, C. A. 2000, *MNRAS*, **315**, 543

- Hurley, J. R., Tout, C. A., & Pols, O. R. 2002, *MNRAS*, **329**, 897
- Kalogera, V., & Baym, G. 1996, *ApJL*, **470**, 61
- Kasen, D., Metzger, B., Barnes, J., Quataert, E., & Ramirez-Ruiz, E. 2017, *Natur*, **551**, 80
- Kiziltan, B., Kottas, A., de Yoreo, M., & Thorsett, S. E. 2013, *ApJ*, **778**, 66
- Kreidberg, L., Bailyn, C. D., Farr, W. M., & Kalogera, V. 2012, *ApJ*, **757**, 36
- Kremer, K., Ye, C. S., Rui, N. Z., et al. 2019, *ApJS*, **247**, 48
- Kruckow, M. U. 2020, *A&A*, **639**, A123
- Kruckow, M. U., Tauris, T. M., Langer, N., Kramer, M., & Izzard, R. G. 2018, *MNRAS*, **481**, 1908
- Lattimer, J. M., & Yahil, A. 1989, *AJ*, **340**, 426
- Lin, J., Rappaport, S., Podsiadlowski, P., et al. 2011, *ApJ*, **732**, 2
- Madau, P., & Fragos, T. 2017, *ApJ*, **840**, 39
- Mandel, I., Mueller, B., Riley, J., et al. 2020, arXiv:2007.03890
- Mandel, I., & Müller, B. 2020, arXiv:2006.08360
- Mapelli, M., & Giacobbo, N. 2018, *MNRAS*, **479**, 4391
- Mapelli, M., Giacobbo, N., Santoliquido, F., & Artale, M. C. 2019, *MNRAS*, **487**, 2
- Marchant, P., Renzo, M., Farmer, R., et al. 2019, *ApJ*, **882**, 36
- Margalit, B., & Metzger, B. D. 2017, *ApJL*, **850**, L19
- McKernan, B., Ford, K. E. S., Bartos, I., et al. 2019, *ApJL*, **884**, L50
- McKinney, W. 2010, in Proc. 9th Python in Science Conf., ed. S. van der Walt & J. Millman, 56, <http://pandas.sourceforge.net>
- Miller, M. C., Lamb, F. K., Dittmann, A. J., et al. 2019, *ApJL*, **887**, L24
- Miller, M. C., & Miller, J. M. 2015, *PhR*, **548**, 1
- Moe, M., & di Stefano, R. 2017, *ApJS*, **230**, 55
- Müller, B., Heger, A., Liptai, D., & Cameron, J. B. 2016, *MNRAS*, **460**, 742
- Müller, H., & Serot, B. D. 1996, *NuPhA*, **606**, 508
- Neijssel, C. J., Vigna-Gómez, A., Stevenson, S., et al. 2019, *MNRAS*, **490**, 3740
- Nitz, A. H., Capano, C., Nielsen, A. B., et al. 2019, *ApJ*, **872**, 195
- Nitz, A. H., Dent, T., Davies, G. S., et al. 2020, *ApJ*, **891**, 123
- Olejak, A., Belczynski, K., Holz, D. E., et al. 2020, arXiv:2004.11866
- Oliphant, T. E. 2006, A Guide to NumPy (USA: Trelgol Publishing), <https://web.mit.edu/dvp/Public/numpybook.pdf>
- Özel, F., Psaltis, D., Narayan, R., & McClintock, J. E. 2010, *ApJ*, **725**, 1918
- Özel, F., Psaltis, D., Narayan, R., & Santos Villareal, A. 2012, *ApJ*, **757**, 55
- Patton, R. A., & Sukhbold, T. 2020, arXiv:2005.03055
- Pérez, F., & Granger, B. E. 2007, *CSE*, **9**, 21
- Petrovich, C., & Antonini, F. 2017, *ApJ*, **846**, 146
- Pfahl, E., Rappaport, S. A., & Podsiadlowski, P. 2003, *ApJ*, **597**, 1036
- Podsiadlowski, P., Langer, N., Poelarends, a. J. T., et al. 2004, *ApJ*, **612**, 1044
- Rastello, S., Mapelli, M., di Carlo, U. N., et al. 2020, arXiv:2003.02277
- Rhoades, C. E., & Ruffini, R. 1974, *PhRvL*, **32**, 324
- Riley, T. E., Watts, A. L., Bogdanov, S., et al. 2019, *ApJL*, **887**, L21
- Rodriguez, C. L., Chatterjee, S., & Rasio, F. A. 2016, *PhRvD*, **93**, 084029
- Rodriguez, C. L., Zevin, M., Amaro-Seoane, P., et al. 2019, *PhRvD*, **100**, 43027
- Romero-Shaw, I. M., Farrow, N., Stevenson, S., Thrane, E., & Zhu, X.-J. 2020, *MNRAS: Letters*, **69**, 64
- Safarzadeh, M., Hamers, A. S., Loeb, A., & Berger, E. 2019, *ApJL*, **888**, L3
- Safarzadeh, M., Ramirez-Ruiz, E., & Berger, E. 2020, arXiv:2001.04502
- Samsing, J., & Hotokezaka, K. 2020, arXiv:2006.09744
- Sana, H., de Mink, S. E., de Koter, A., et al. 2012, *Sci*, **337**, 444
- Santoliquido, F., Mapelli, M., Bouffanais, Y., et al. 2020, arXiv:2004.09533
- Schroeder, G., Margalit, B., Fong, W.-F., et al. 2020, arXiv:2006.07434
- Sigurdsson, S., & Hernquist, L. 1993, *Natur*, **364**, 423
- Silsbee, K., & Tremaine, S. 2017, *ApJ*, **836**, 39
- Spera, M., Mapelli, M., Giacobbo, N., et al. 2019, *MNRAS*, **485**, 889
- Stephan, A. P., Naoz, S., Ghez, A. M., et al. 2019, *ApJ*, **878**, 58
- Stevenson, S., Berry, C. P. L., & Mandel, I. 2017, *MNRAS*, **2811**, 2801
- Taam, R. E., & Sandquist, E. L. 2000, *ARA&A*, **38**, 113
- Talbot, C., & Thrane, E. 2017, *PhRvD*, **96**, 023012
- Tauris, T. M., Langer, N., & Kramer, M. 2011, *MNRAS*, **416**, 2130
- Tauris, T. M., Langer, N., & Podsiadlowski, P. 2015, *MNRAS*, **451**, 2123
- Thompson, T. A., Kochanek, C. S., Stanek, K. Z., et al. 2019, *Sci*, **366**, 637
- van den Heuvel, E. P. 2007, in AIP Conf. Proc. 924, The Multicolored Landscape of Compact Objects and Their Explosive Origins, ed. L. A. Antonelli et al. (Melville, NY: AIP), 598
- van den Heuvel, E. P. J., & Tauris, T. M. 2020, *Sci*, **368**, eaba3282
- van der Walt, S., Colbert, S. C., & Varoquaux, G. 2011, *CSE*, **13**, 22
- Venumadhav, T., Zackay, B., Roulet, J., Dai, L., & Zaldarriaga, M. 2019, *PhRvD*, **100**, 23011
- Venumadhav, T., Zackay, B., Roulet, J., Dai, L., & Zaldarriaga, M. 2020, *PhRvD*, **101**, 83030
- Vigna-Gómez, A., Neijssel, C. J., Stevenson, S., et al. 2018, *MNRAS*, **481**, 4009
- Villar, V. A., Guillochon, J., Berger, E., et al. 2017, *ApJL*, **851**, L21
- Vink, J. S., & de Koter, A. 2005, *A&A*, **442**, 587
- Vink, J. S., de Koter, A., & Lamers, H. J. G. L. M. 2001, *A&A*, **369**, 574
- Virtanen, P., Gommers, R., Oliphant, T. E., et al. 2020, *NatMe*, **17**, 261
- Vitale, S., Lynch, R., Sturani, R., & Graff, P. 2017, *CQGra*, **34**, 03LT01
- Webbink, R. 1984, *ApJ*, **277**, 355
- Woosley, S. E. 2017, *ApJ*, **836**, 244
- Woosley, S. E. 2019, *ApJ*, **878**, 49
- Wyrzykowski, Ł., & Mandel, I. 2020, *A&A*, **636**, 1
- Yang, Y., Bartos, I., Haiman, Z., et al. 2019, *ApJ*, **876**, 122
- Ye, C. S., Fong, W.-F., Kremer, K., et al. 2020, *ApJL*, **888**, L10
- Yoon, S. C., & Langer, N. 2005, *A&A*, **443**, 643
- Zevin, M., Kremer, K., Siegel, D. M., et al. 2019, *ApJ*, **886**, 4
- Zevin, M., Pankow, C., Rodriguez, C. L., et al. 2017, *ApJ*, **846**, 82